IEEE Access
Multidisciplinary ⋮ Rapid Review ⋮ Open Access Journal

Received 26 April 2023, accepted 15 May 2023, date of publication 23 May 2023, date of current version 19 July 2023.

Digital Object Identifier 10.1109/ACCESS.2023.3279277

RESEARCH ARTICLE

Multi-Objective Optimization Design of Assembled Wheel Lightweight Based on Implicit Parametric Method and Modified NSGA-II

SHUAI ZHANG[1], RUIXU LI[1], DONGZHEN LU[1], LIYOU XU[1], AND WENCHAO XU[2,3]

[1]College of Vehicle and Traffic Engineering, Henan University of Science and Technology, Luoyang 471003, China
[2]College of Automobile Engineering, Jilin University, Changchun 130022, China
[3]State Key Laboratory of Automotive Simulation and Control, Jilin University, Changchun 130022, China

Corresponding author: Liyou Xu (xlyou@haust.edu.cn)

This work was supported in part by the Major Science and Technology Project of Henan Province under Grant 221100240400, in part by the Key Research and Development and Promotion Project of Henan Province under Grant 232102240052, and in part by the National Key Research and Development Program of China under Grant 2022YFD2001203.

ABSTRACT To improve the fatigue life of the wheel, the level of lightweight design, and the efficiency and accuracy of optimization analysis. In this paper, a wheel finite element analysis model combining shell-body elements is established, and a design and optimization method for an assembled wheel with a magnesium alloy rim-aluminum alloy spoke structure is proposed. Based on the advanced grid deformation technology and implicit parameterization technology, the assembled wheel fatigue analysis parametric model is created, DOE sampling is carried out, and the design variables are screened out by combining the contribution analysis method. A hybrid method of entropy weighted grey relation analysis (EGRA) combined with modified non-dominated sorting genetic algorithm-II (MNSGA-II) is proposed for multi-objective optimization of the assembled wheel in combination with an approximate model approach to obtain the Pareto frontier solution set and its grey relation order to filter the preferred compromise solution. The simulation analysis compares and optimizes various performance indicators of the front and rear assembled wheels, and is verified by bending and radial fatigue tests. The results show that the weight of the wheel is reduced by 10.17%, and the weight reduction effect is remarkable. Under the condition of ensuring the calculation accuracy, the wheel shell-volume element combination model proposed in this paper saves at least 46.44% of the calculation time compared with the volume element model.

INDEX TERMS Assembled wheel, shell-body element combination, bending and radial fatigue performance, entropy-weighted grey relation analysis, lightweight multi-objective optimization.

I. INTRODUCTION

Lightweighting technology is the most effective means to improve the overall performance of vehicles and achieve energy saving and emission reduction [1], [2]. As an essential safety and load-bearing part of the car, the wheel's lightweight level and fatigue durability directly affect the car's safety, power, fuel economy, and braking performance [3], [4]. It is of great scientific significance and engineering prospect to construct a set of multi-objective lightweight design methods for wheels to achieve lightweighting and solve the critical problems in wheel development and design under the premise of meeting all requirements.

Domestic and foreign scholars have proposed different approaches and paths in wheel lightweight. In terms of high-strength lightweight materials, applying high-strength steel, aluminum alloy, magnesium alloy, and carbon fiber composite materials is the most efficient solution to achieve a lightweight wheel. Wang et al. [5] designed a heterogeneous steel wheel with high-strength steel as the inner rim and mild steel as the outer rim material and achieved a

The associate editor coordinating the review of this manuscript and approving it for publication was Sudhakar Babu Thanikanti.

9.73% weight reduction in wheel mass by comparing before and after optimization. Jiang et al. [6] established a finite element analysis model for magnesium alloy wheels. They performed a dynamic impact simulation analysis, and the comparison showed that the target weight reduction of 32.3% was achieved. Xu and Wang [7] proposed a carbon fiber reinforced polymer rim structure, simulated and analyzed the bending and radial fatigue strength of the wheel, and conducted fabrication tests on the optimized wheel. The data results all met the standard requirements. Zhang and Xiao [8] improved the aluminum alloy wheel because the permissible stress and the inherent frequency of the wheel were satisfied, and the test results showed a 13.9% reduction in wheel weight. Czypionka and Kienhofer [9] used carbon fiber material instead of aluminum wheels, and optimization models showed that carbon fiber material could reduce the weight of the wheels by 18%.

Compared with the cost increase of lightweight materials, the optimized design of the wheel structure lightweight plays an essential role in improving the efficiency of component development, saving costs, and improving component performance. The traditional structural optimization design methods are difficult to describe accurately for the complex structure of the components, limiting the optimization design results. The parametric modeling technology can achieve the goal of lightweight, optimized design by changing the shape parameters of the components. At present, mesh deformation technology and implicit parameterization technology are widely used in automobile lightweight. Wang and Cheng [10] proposed an adaptive refinement mesh technique by actin

g on the local mesh to be deformed to calculate the deformation offset shape variables, which effectively solves the problems of insufficient mesh vertices and mesh density. Fang et al. [11] proposed a mesh deformation method based on a Cartesian background network (MDCBM), which can quickly complete mesh deformation, improve computational efficiency and obtain high-quality deformed meshes. Xie et al. [12] proposed a double constrained radial basis function (RBF) interpolation algorithm that does not require moving the mesh nodes near the stationary boundary and effectively improves the efficiency of mesh deformation. Wang et al. [13] proposed a wheel optimization design method based on the fatigue, 13° impact, and 90° impact performance of the wheel. 12 design variables were defined, and a parametric model of the wheel was established using the grid deformation technique, and the optimized wheel mass was reduced by 28.59%, which provided a theoretical and technical basis for wheel optimization design. Duan et al. [14] proposed an implicit parameterization, global sensitivity analysis (GSA) and Pareto set pursuing (PSP) light-weighting strategy. The strategy can generate uniformly distributed Pareto optimal fronts and reduce the complexity of body-in-white light-weighting design. Wang et al. [15] analyzed and calculated the low-order intrinsic vibration frequencies and modes of the body-in-white (BIW) by developing an implicit parametric model and a body-in-white (BIW) finite element model. The results show that the implicit parametric model can be used in the body-in-white design development stage. Chen et al. [16] proposed an implicit parametric model integrated with a multidisciplinary design optimization method, which can realize automatic modification and fast multidisciplinary optimization design to improve computational efficiency and material utilization. Yao et al. [17] developed an implicit parametric model of a typical body-in-prime (BIP) body structure by using SFE-Concept software to optimize the beam structure parameters and improve dynamic static performance without significant mass increase. Liu et al. [18] used SFE-Concept software to construct a mathematical model of the SUV chassis structure with implicit parametric modeling to explore and optimize a more extensive range of structures rapidly.

In the selection of multi-objective optimization algorithms, traditional optimization algorithms are challenging to solve multi-objective optimization problems and have limitations. Non-dominated sorting genetic algorithm-II NSGA-II is one of the most popular multi-objective genetic algorithms. The quick dominance sorting algorithm is proposed in NSGA-II, which can reduce the complexity of the calculation. Bora et al. [19] present an improved non-dominated sorting genetic algorithm II (NSGA-II) approach incorporating a parameter-free self-tuning by reinforcement learning technique called learner non-dominated sorting genetic algorithm (NSGA-RL) for the multi-objective optimization of the environmental/economic dispatch (EED) problem. Akbari et al. [20] the microstructural and mechanical properties of B4C/A356 composites were optimized using artificial neural network (ANN) and non-dominated sorting genetic algorithm-II (NSGA-II). Research shows a modified NSGA-II incorporating a diversity preserving mechanism called the elimination algorithm was employed to obtain the Pareto-optimal set of FSP parameters. Xu et al. [21] used a modified non-dominated sorting genetic algorithm-II (MNSGA-II) to improve the convergence of the multi-objective algorithm and further reduce the uncertainty optimization of the transportation equipment to reduce the risk of failure. Xiong et al. [22] used a combined MNSGA-II and ideal point method (IPM) approach for crashworthiness and multi-objective light-weighting optimization of body-side structures. In multi-objective optimization design, multiple optimization methods are usually combined to obtain the optimal design scheme. While improving the overall crashworthiness of the car and ensuring the rigidity of the body, the side structure of the body is optimized to reduce the weight by 4.18kg. Wang et al. [23] proposed non-dominated sorting genetic algorithm-II (NSGA-II) and Technique for ordering preferences by similarity to ideal solution (TOPSIS) method for the lightweight optimization design of the front subframe of a sedan. They used entropy power theory and TOPSIS method to rank the solutions and determine the best design solution. Xiong et al. [24]

used entropy-weighted grey relation analysis (EGRA) for multi-objective optimization of the front-end body structure. EGRA determined the optimal combination of thickness and material parameters for the optimized part, and the optimization results showed a 4.98 kg reduction in body mass. At the same time, the first-order torsional frequency, first-order bending frequency and bending stiffness increased by 0.14%, 0.92% and 0.20% respectively, while the torsional stiffness decreased by 0.30%, which verified the effectiveness of lightweight optimization. Zhang et al. [25] proposed an entropy-weighted grey relation analysis (EGRA) wheel lightweighting multi-objective optimization method using EGRA to obtain the optimal design solution with a 10.83% reduction in assembled wheel mass and 32.74% mass reduction with the same type of cast aluminum alloy wheels.

The wheel is a structural and load-bearing part of the automobile chassis, and the fatigue performance of the wheel has always been a research focus for researchers. Currently, the fatigue life analysis method for monolithic metallic wheels is relatively mature, and many research scholars have conducted a lot of studies. Zhao et al. [26] conducted fatigue tests on the rims of AZ80 wheels to study the fatigue performance of the wheels and to provide a theoretical basis for the fatigue-resistant design of magnesium alloy wheels. Shang et al. [27] predicted the fatigue life of steel wheels based on the residual stresses of stamping and forming and a superimposed the residual stresses during stamping and bending fatigue stresses, which effectively improved the validity and accuracy of predicting the bending fatigue life of wheels. Jiang et al. [28] calculated the maximum stress of the steel wheel with and without superimposed residual stress field. They predicted the fatigue life of the steel wheel by establishing a simulation model. The simulation results showed that the maximum stress before and after the superimposed residual stress appeared at the bottom of the groove, which was consistent with the actual failure location. The research results provided a theoretical basis for the lightweight design of the steel wheel. Wan et al. [29] proposed a new method for wheel fatigue life by establishing a wheel fatigue test bench model based on the standard, conducting biaxial wheel tests and fatigue life estimation, and comparing the simulation results with the test results to predict the fatigue life of wheel biaxial tests more effectively. Duan et al. [30] proposed a multi-scale biaxial fatigue test method with significantly improved prediction results, which laid the foundation for optimal design and fatigue prediction of aluminum alloy wheels. Chen et al. [31] used Wheel-Strength software to predict wheel bending and radial fatigue life. The fatigue test results showed that the lightweight design requirements were met with a 14% reduction in rim weight. Compared with all-metal wheels, the fatigue life analysis of assembled metal wheels is relatively complicated. There are relatively few studies on the fatigue life analysis of assembled metal wheels at home and abroad. Wang and Xu [32] analyzed the fatigue life of the discs, rims, connecting bolts, and structural glue of the aluminum/magnesium alloy assembled wheel connected by glue bolts and carried out an integrated multi-objective optimization design based on the structure-bending fatigue life of the wheel.

The above studies have improved the lightweight level of wheels from materials, optimization algorithms, and fatigue analysis, but most focus on all-metal integral wheels. Based on the above research and the implicit parameterization method, the 16 × 6½J-type wheel is taken as the research object in this paper. The 16 × 6½J-type wheel is taken as the research object in this paper. An assembled wheel with a magnesium alloy rim-aluminum alloy spoke structure is designed by establishing the finite element analysis model of the wheel combined with the shell-body element. We are considering the impact of different metal materials and fatigue conditions. The performance impact of assembled wheels, combined with contribution analysis, surrogate model, Design of Experiment (DOE), and entropy-weighted grey relation analysis (EGRA) methods, using the modified non-dominated sorting genetic algorithm-II (MNSGA-II) for multi-objective optimization design of assembled wheels, for lightweight assembly The development of the wheel provides theoretical and technical basis.

II. METHODOLOGY

A. ENTROPY-WEIGHTED GREY RELATION ANALYSIS

The grey relation method based on entropy weight is adopted., which not only retains the advantages of the entropy method of using information entropy to measure the weight of indicators but also maximizes the advantages of the grey relation analysis method. The steps are as follows:

Step1: Grey relational generation

The grey relational generation for different characteristic quotas differs from each other

(a) If the objective has the characteristic of 'the larger, the better', then the normalization method can be expressed as:

$$x_i^*(k) = \frac{x_i(k) - \min_k x_i(k)}{\max_k x_i(k) - \min_k x_i(k)} \tag{1}$$

(b) If the objective has the characteristic of 'the lower, the better', then the normalization method can be expressed as:

$$x_i^*(k) = \frac{\max_k x_i(k) - x_i(k)}{\max_k x_i(k) - \min_k x_i(k)} \tag{2}$$

(c) If the objective has the characteristic of 'closer to a specific value, the better the performance', then the normalization method can be expressed as:

$$x_i^*(k) = 1 - \frac{|x_i(k) - T|}{\max\left[\max_k x_i(k) - T, T - \min_k x_i(k)\right]} \tag{3}$$

where $x_i*(k)$ and $x_i(k)$ are the regularized and initial values of the kth objective function at the ith scenario (design variable), respectively; $min_k\ x_i(k)$ and $max_k\ x_i(k)$ is the maximum and minimum values of the kth objective function in all schemes, respectively; T is a specific value.

Step2: Calculate the grey relation coefficient (GRC)

$$\gamma\left(x_0^*(k), x_i^*(k)\right) = \frac{\Delta_{\min} + \zeta\Delta_{\max}}{\Delta_{0i}(k) + \zeta\Delta_{\max}} \tag{4}$$

where $\Delta_{0i}(k) = |x_0^*(k) - x_i^*(k)|$, $x_0^*(k)$ is the normalization value of the kth objective function in the case of an ideal scheme; Δ_{max} and Δ_{min} is the maximum and minimum values of $\Delta_{0i}(k)$; ξ, discrimination coefficient, is defined as 0.5 in the article.

Step3: Calculate the grey relation grade (GRG)

$$\Gamma\left(x_0^*, x_i^*\right) = \sum_{k=1}^{n} \omega_k \gamma\left(x_0^*(k), x_i^*(k)\right) \tag{5}$$

where ω_k is the weight coefficient of the kth objective function; n is the number of objective functions; $(\sum_{k=1}^{n} \omega_k = 1)$

Step4: Calculating the weight according to the entropy weight (EW) method

(a) Normalizing the data.

$$r_i = \frac{x_i(k)}{\sqrt{\sum_{i=1}^{M} (x_i(k))^2}} \tag{6}$$

where r_i is the normalization result of $x_i(k)$.

(b) Calculating the information entropy.

The information entropy of the optimization quota is calculated using equation

$$e_j = -\frac{1}{\ln m} \sum_{i=1}^{m} \left[\frac{r_i}{\sum_{i=1}^{m} r_i} \cdot \ln \frac{r_i}{\sum_{i=1}^{m} r_i} \right] \tag{7}$$

where e_j is the information entropy of the jth optimization quota ($e_j \in [0, 1]$).

(c) Calculating the information utility value.

The calculation formula of information utility value d_j is as follows:

$$d_j = 1 - e_j \tag{8}$$

where d_j is information utility value; e_j is information entropy.

(d) Calculating weights coefficient.

The weights coefficient of the optimization of the optimization quota is calculated using equation

$$\omega_k = \frac{1 - e_k}{\sum_{k=1}^{n} (1 - e_k)} \tag{9}$$

where ω_k represents the weight of the jth optimization quota ($\omega_k \in [0, 1]$; $\Sigma_{k=1}^{n} \omega_k = 1$).

B. RBF APPROXIMATE MODEL

RBF simulates the relationship between input variables (such as design variables) and responses with linear combinations of radial symmetric functions based on Euclidean distances [33].

From Fig 1, the RBF is divided into three main layers. Among them, the input layer is mainly used to introduce variable information, the implicit layer is responsible for mapping the input information to the output layer according to specific mathematical relationships, and the output layer is responsible for weighting the outputs of the nodes in the implicit layer. It can be expressed as follows:

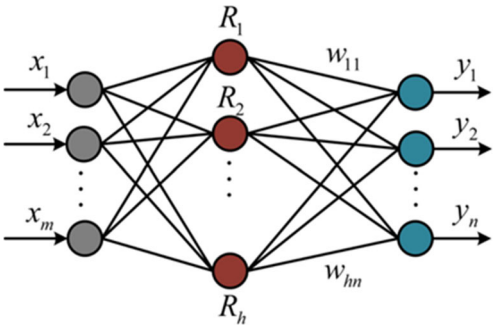

FIGURE 1. Structure diagram of RBF.

$$\hat{y}_j(x) = \sum_{k=1}^{m} w_{ij} \|x - x_k\| \tag{10}$$

where $\hat{y}_j(x)$ is the jth response approximation, n is the number of output responses; w_{ij} is the connection weight between the ith hidden layer node and the jth output layer node; $\|x - x_k\|$ denotes the distance between sample x and the kth sample x_k in the design space, and m is the number of design variables.

C. KRIGING APPROXIMATE MODEL

The Kriging approximation model is highly accurate in solving highly nonlinear problems and is widely used in engineering [34]. The expressions are:

$$\hat{y}(x) = f^T(x) \cdot \beta + z(x) \tag{11}$$

where $f^T(x)$ is a polynomial with a design vector x; β is the vector of regression coefficients, $\beta = [\beta_1, \beta_2, \ldots, \beta_n]^T$; $z(x)$ is the random deviation. $z(x)$ is a random function with mean zero and standard deviation σ. The covariance is:

$$cov\left[z(x_i), z(x_j)\right] = \sigma^2 R\left(\left[R(x_i, x_j)\right]\right) \tag{12}$$

where R is an $n \times n$ symmetric relation matrix of order 1 on both diagonals; $R(x_i, x_j)$ is the relation function of any two sampling points x_i and x_j in the n training samples.

Using the Gaussian relation function $R(x_i, x_j)$ can be expressed as:

$$R(x_i, x_j) = EXP\left(-\sum_{k=1}^{m} \theta_k \left| x_{ik} - x_{jk} \right|^2 \right) \tag{13}$$

where m is the number of design variables; θ_k is the relation coefficient used to fit the approximate model; x_{ik} and x_{jk} are the kth elements of sample points x_i and x_j, respectively.

D. MODIFIED NSGA-II

Compared with NSGA-II, MNSGA-II uses a fixed threshold ε-elimination strategy to better handle population diversity for multi-objective optimization problems, Therefore, this method is used to solve the multi-objective optimization

problem in a more scientific way. The process is shown in Fig 2. the MNSGA-II algorithm operates as follows.

The steps of MNSGA-II algorithm are as follows:

Step 1: Generate a parent population P_t with population number N and non-dominated sorting of all individuals in it.

Step 2: Selection, crossover and mutation of sorted individuals to produce the next generation of populations Q_t.

Step 3: Merging parent population P_t and offspring population Q_t,, obtain a mixed population R_t with population number R_t and non-dominated sorting of the individuals of the mixed population $2N$.

Step 4 According to the fixed threshold ε-elimination strategy, undesirable individuals are removed from the mixed population R_t and then random individuals are generated to fill the population R_t so that its population number remains constant in size $2N$.

Step 5 Perform an undominated sorting operation on the population R_t according to the undominated sorting criteria. m $(m>N)$ superior individuals were selected sequentially from the lower to the higher levels, and then a fixed threshold ε-elimination was performed until a population number N parent population P_{t+1} was obtained.

Step 6 If the termination condition is satisfied, the iteration ends, otherwise the optimization is repeated from step 2 until the non-dominated solution satisfies the termination condition.

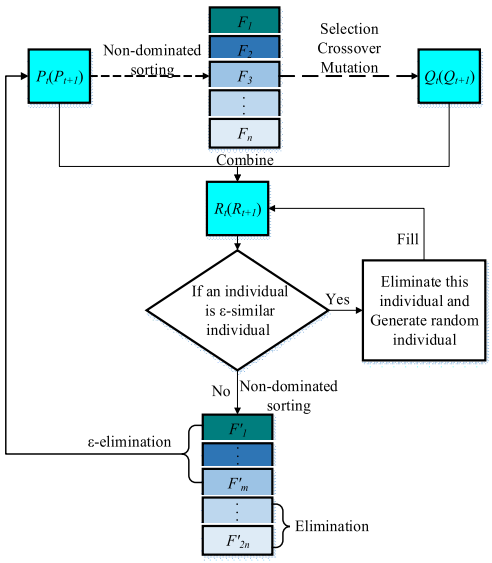

FIGURE 2. The principle of modified NGSA-II algorithm.

III. DISC TOPOLOGY OPTIMIZATION AND ASSEMBLED WHEEL MODELING

A. CONCEPTUAL DESIGN MODEL of WHEEL TOPOLOGY OPTIMIZATION

In this paper, 16 × 6$^1/_2$J-type wheel is taken as the research object. The assembled wheel is designed by using the topology optimization method and multi-objective optimization method. The disc and rim are made of aluminum alloy and magnesium alloy, respectively, and are connected by bolts. The rim design belongs to the detailed design stage of the wheel, and the detailed design and multi-objective optimization are carried out after the implicit parametric modeling of the rim. In the conceptual design stage of the wheel, only the disc structure is optimized. The topology optimization space of the disc is filled with entities, and the conceptual design model is shown in Fig. 3.

FIGURE 3. Wheel conceptual design model.

B. DISC TOPOLOGY OPTIMIZATION MODEL BASED ON BENDING FATIGUE TEST

The conceptual wheel design model was imported into the pre-processing software Hypermesh for geometric cleaning, and the wheel model was meshed with tetrahedral elements. The element size of both rim and disc topological space is 5mm, and the element size of the loading arm is 10mm, allowing a minimum size of 2mm. The rim and disc parts of the assembled wheel are given the material properties of magnesium alloy ZK61M and aluminum alloy 6061, respectively. The length of the load arm is taken as 1m and given the material properties of A_3 steel. The material parameters of each part of the wheel model are given in Table 1, and the strength parameters of the rim and disc are given in Table 2.

TABLE 1. Material parameters of wheel rim and disc.

Material	Density ρ (t/mm^3)	Elastic modulus E (MPa)	Poisson ratio μ
ZK61M	1.78×10-9	4.5×104	0.35
6061	2.7×10-9	6.9×104	0.33
A3	7.9×10-9	2.1×105	0.30

TABLE 2. Strength parameters of rim and disc.

Material	Tensile strength /MPa	Yield strength /MPa	Allowable tensile strength /MPa	Allowable yield strength /MPa
ZK61M	258	170	215	141.2
6061	282	190	235	158.3

When structural design and finite element analysis are carried out, the safety factor is used to calculate the allowable strength of the material so as to ensure the strength margin and reliability of the structure. According to experience, the safety factor s is taken as 1.2 to calculate the allowable strength of

magnesium and aluminum alloy. The wheels in this paper are processed by the forging process. Table 2 shows the strength parameters of the forged ZK61M magnesium alloy rim and 6061 aluminum alloy spokes.

The wheel finite element model is discretized into a total of 218613 elements and 56783 nodes. A constraint is applied to the nodes along the outer edge of the inner wheel rim to constrain all its degrees of freedom. The topologically optimized finite element model of the wheel under bending fatigue conditions established by applying a force of 2472 N at the end of the loaded axle is shown in Fig 4.

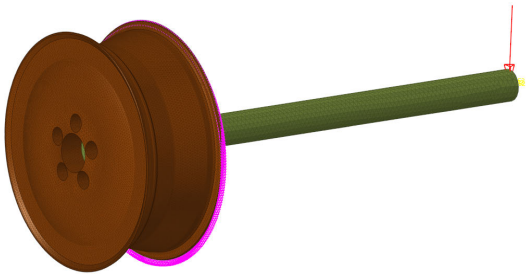

FIGURE 4. Topology optimization model of wheel bending fatigue condition.

C. DISC TOPOLOGY OPTIMIZATION MODEL BASED ON RADIAL FATIGUE TEST

The conceptual wheel design model for radial fatigue conditions was imported into Hypermesh for finite element pre-processing. Constraints are applied to the nodes of the 5 bolt holes within the wheel mounting surface, constraining all degrees of freedom. A cosine pressure with an amplitude of 1.76MPa is loaded within the bead seat $2\theta_0$ angle, and an inflation pressure of 0.45MPa is applied to the outer surface element between the two bead seats of the tire. As shown in Fig. 5.

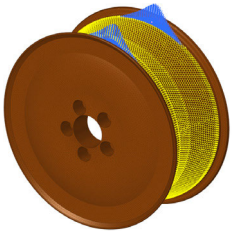

FIGURE 5. Topology optimization model of wheel radial fatigue condition.

D. JOINT TOPOLOGY OPTIMIZATION AND DESIGN of ASSEMBLED WHEELS

1) COMBINED TWO OPERATING CONDITIONS DISC TOPOLOGY OPTIMIZATION

In natural road conditions, the wheel cannot always be in a single working condition, so optimizing the disc topology in a single operating condition is inadequate. Therefore, after importing the wheel topology optimized finite element model into Optistruct, two composite conditions, bending and radial loading, need to be added to make the topology more reasonable.

Therefore, the topology optimization model of the wheel bending fatigue condition shown in Figure 4 is imported into Optistruct. the load condition in Figure 5 is added to perform joint topology optimization of the tire. The mathematical model is:

$$\begin{cases} \min(m(\boldsymbol{\rho})) \\ s.t. \begin{cases} \sigma_{bd}(\boldsymbol{\rho}) \le \sigma_d \\ \sigma_{br}(\boldsymbol{\rho}) \le \sigma_r \\ D_b(\boldsymbol{\rho}) \le D_{b0} \\ \sigma_{rd}(\boldsymbol{\rho}) \le \sigma_d \\ \sigma_{rr}(\boldsymbol{\rho}) \le \sigma_r \\ |C_r(\boldsymbol{\rho}) - C_{r0}| \le 0.15 C_{r0} \\ \boldsymbol{\rho} \in (0, 1) \end{cases} \end{cases} \tag{14}$$

where $m(\boldsymbol{\rho})$ is the wheel mass (t), $\sigma_{bd}(\boldsymbol{\rho})$ is the maximum Von Mises stress of disc in the bending fatigue conditions (MPa); σ_{d} is the allowable yield stress of disc (MPa), $\sigma_{\mathrm{d}} = 158.3Mpa$;$\sigma_{br}(\boldsymbol{\rho})$ is the maximum Von Mises stress of rim in the bending fatigue conditions (MPa); σ_{r} is the allowable yield stress of rim (MPa), $\sigma_{\mathrm{r}} = 141.2MPa$;$D_b(\boldsymbol{\rho})$ is the maximum wheel nodes offset in the bending fatigue conditions (mm); ;$\mathrm{D_{b0}}$ is the allowable nodes offset (mm), $\mathrm{D_{b0}} = 0.8mm$; $\sigma_{rd}(\boldsymbol{\rho})$ is the maximum Von Mises stress of disc in the radial fatigue conditions (MPa);$\sigma_{rr}(\boldsymbol{\rho})$ is the maximum Von Mises stress of rim in the radial fatigue conditions (MPa); $C_r(\boldsymbol{\rho})$ is the weighted compliance of wheel in the radial fatigue conditions N·mm; $\mathrm{C_{r0}}$ is the allowable compliance, N·mm; $\mathrm{C_{r0}} = 3800N \cdot mm$, $\boldsymbol{\rho}$ is the element density, $\mathrm{t/mm^3}$.

Then it was submitted to the Optistruct solver and solved with the minimum wheel mass as the optimization objective, and the relative density threshold was set to 0.3. The optimization results are shown in Figure 6.

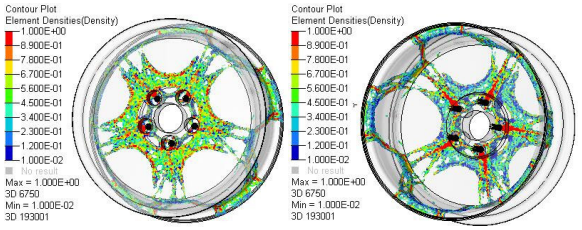

(a) Front side of the wheel (b) Reverse side of the wheel

FIGURE 6. Joint topology optimization result.

Under the joint topology optimization, the wheel material distribution and density magnitude are influenced by both test conditions. The dynamic bending fatigue test significantly affects the topology of the disc roots, and the radial fatigue test significantly affects the topology of the rim and disc joint. The optimization results show that the results of the optimized wheel topology are reasonable, and the topology is selected for the design and modeling of the wheel.

2) ASSEMBLED WHEEL STRUCTURE DESIGN

The topology of the five-spoke wheel after the joint topology optimization is imported into the post-processing software Hyperview. The wheel topology is derived using the OSSmooth tool. After smoothing, the three-dimensional model of the wheel after the joint topology optimization is obtained. Based on the dimensions of this geometric model, the 3D model of the assembled wheel after topology optimization was created in UG, as shown in Fig 7.

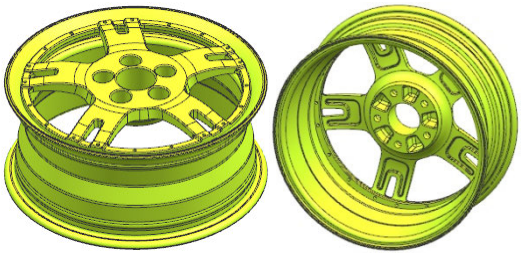

(a) Front side of the wheel (b) Reverse side of the wheel

FIGURE 7. 3D model of the assembled wheel.

E. PARAMETRIC MODELING OF ASSEMBLED WHEELS

1) RIM IMPLICIT PARAMETRIC MODELING TECHNOLOGY

To reduce the calculation time, the rim is extracted from the center surface and divided into meshes using SFE-Concept software to build an implicit parametric model of the rim. The implicit parametric modeling process of the wheel rim is shown in Fig 8

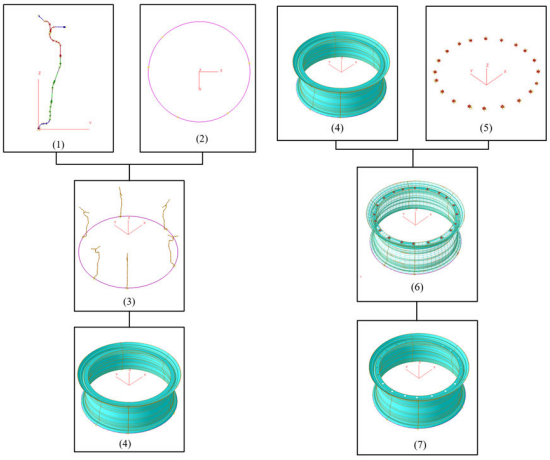

(a) Rim body parametric modeling (b) Rim bolt hole parametric modeling

FIGURE 8. Rim implicit parametric modeling process.

As shown in Fig 8(a), The rim section parameterization curve (1) and the swept path (2) are established according to the finite element model, and the two are combined to form (3) after adding control nodes and (4) after circular sweeping.

The bolt holes are parametrically modeled separately, as shown in Fig 8(b). Locate the position and size of the bolt hole (5), then map it to (4), and the position relationship between the two combined is shown in Fig. (6), and the rim parameterized model (7) is formed after shearing the bolt hole.

The established rim implicit parametric model is shown in Fig 9(a) is the overall picture of the rim, and Fig (b) is the detailed picture of the rim bolt hole. After the parametric rim model is established, the finite element parametric mesh of the rim is automatically generated. The parametric rim model has 19147 shell elements, as shown in Fig 10.

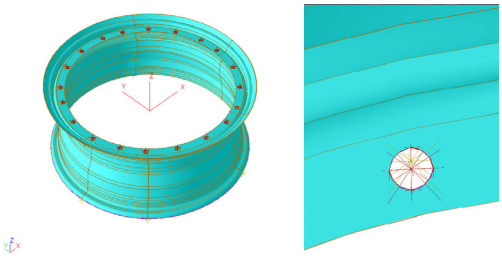

(a) Global graph (b) Detail diagram

FIGURE 9. Rim parametric model.

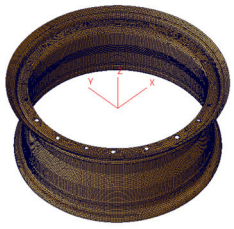

FIGURE 10. Rim finite element parametric mesh.

2) DISC MESH DEFORMATION TECHNICAL PARAMETERIZATION MODELING

To improve the disc's deformation ability and design space and increase the experimental design's sampling space, a parametric design of the disc model is needed. The design disc is a body mesh, and the DEP-Mesh Works software controls the translation and scaling of the mesh model

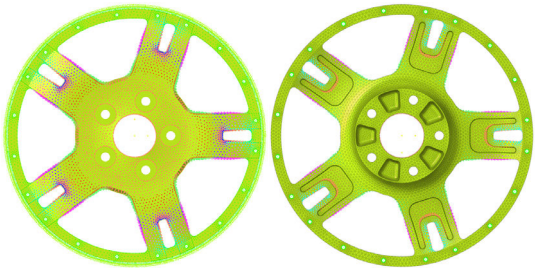

(a) Front side of discs (b) Reverse side of discs

FIGURE 11. Parametric model of wheel spokes.

nodes through advanced mesh deformation techniques. The established parametric model of the wheel discs is shown in Fig. 11.

The parametric models of the rims and discs are assembled together to form a wholly assembled wheel parametric model, as shown in Fig 12.

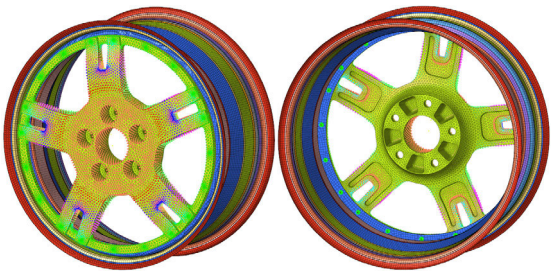

(a) Front side of the wheel (b) Reverse side of wheel

FIGURE 12. Parametric model for rim and disc assembly.

IV. STATIC AND MODAL ANALYSIS OF ASSEMBLED WHEELS

A. ASSEMBLY WHEEL FINITE ELEMENT MODELING

The assembled wheel parametric model is imported into Hypermesh, and the parametric rim model has 19147 shell elements, which is 239741 less than the body element rim model. The parametric rim model has 96606 individual elements. The bolted connections of the rims and discs are simulated using RBE2 elements. The finite element model of the wheel is shown in Fig 13.

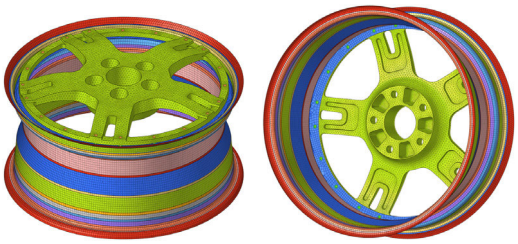

(a) Front side of the wheel (b) Reverse side of the wheel

FIGURE 13. Finite element model of wheels.

B. ANALYSIS OF WHEEL BENDING FATIGUE PERFORMANCE

The wheel bending fatigue condition finite element model is established basically the same as in section B, but the direction of loading force is divided into 3 directions, as shown in Fig 14(b). Among them, F1 corresponds to blue, F2 to red, and F3 to green. Among them: the loading force F1 is facing the window, the loading force F2 is in the middle position, and the loading force F3 is facing the spoke. They are respectively recorded as F1, F2, and F3 working conditions during calculation and analysis. Because the wheel is an axisymmetric structure, the bending load when the wheel rotates to any position can be represented by these three typical working conditions. The finite element model of the assembled wheel bending fatigue test is shown in Fig 14.

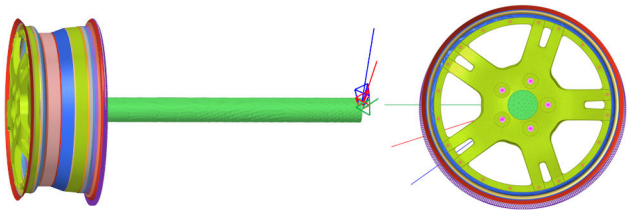

(a) Axonometric drawing (b) Floor plan

FIGURE 14. Finite element analysis model of wheel bending conditions.

The CPU model of the computer is AMD Ryzen 5 3600X 6-Core Processor, its running memory is 15.9 GB, and the simulation results are solved using the default number of cores (single core).

For the reliability of the rim shell element model (collectively referred to as the shell element model later) in fatigue analysis, the results of three working conditions are compared with those of the rim body element (collectively referred to as the body element model later), as shown in Fig 15-18.

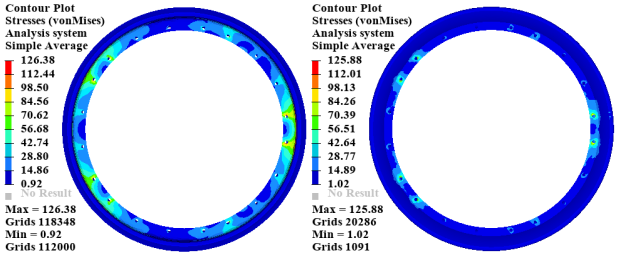

(a) Shell element model (b) Body element model

FIGURE 15. Rim stress under F_1 working condition.

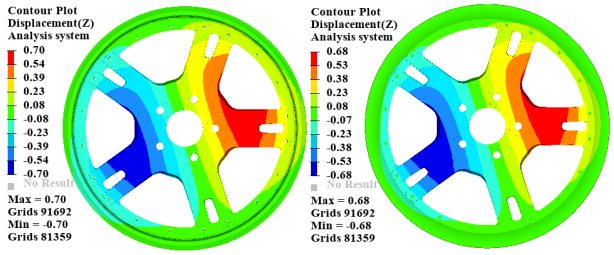

(a) Shell element model (b) Body element model

FIGURE 16. Wheel offset at F_2 working condition.

The simulation calculation shows that the maximum stress on the rim is at the F_1 working condition, and the maximum stress occurs at the bolt hole of the rim ring. The wheel offset is the largest in the F_2 condition, and the nodal displacement at the root of the spokes is the largest. The maximum stress in the discs at the F_3 operating condition occurs at the root weight reduction groove on the opposite side of the spokes,

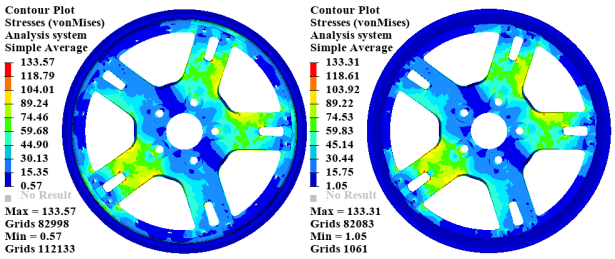

(a) Shell element model (b) Body element model

FIGURE 17. Disc stress at F_3 working condition.

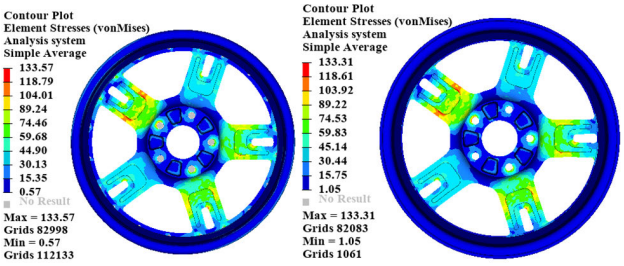

(a) Shell element model (b) Body element model

FIGURE 18. The stress on the opposite side of the disc under F_3 condition.

while the root stress at the front side of the spokes is also higher.

As shown in Figure 15-18. When the loading force faces the window (F1 working condition), the rim stress is the largest and the maximum stress occurs at the bolt hole of the rim ring. When the loading force faces the middle position (F2 working condition), the wheel deflection is the largest, and the most significant nodal displacement occurs at the root of the spoke. When the loading force is directly on the spoke (F3 working condition), the disc stress is the largest, and the maximum stress occurs at the root weight reduction groove on the opposite side of the spokes, while the root stress at the front side of the spokes is also higher.

The comparison results are shown in Table 3. As can be seen from Table 3, regarding the maximum stress on the rim, the maximum offset of the wheel, and the maximum stress on the discs, the new model and the old model not only meet the requirements, the difference between them is less than 5%, as well as the occurrence location, is the same, but the calculation time is reduced by 46.44%.

TABLE 3. Comparison of bending fatigue static performance of shell element model.

Performance	Shell element model	Body element model	Change rate
Maximum rim stress/MPa	126.38	125.88	0.40%
Maximum wheel offset/mm	0.70	0.68	2.94%
Disc maximum stress/MPa	133.57	133.31	0.20%
Calculation time/s	14.82	27.67	-46.44%

C. WHEEL RADIAL FATIGUE PERFORMANCE ANALYSIS

The wheel model is imported into Hypermesh for pre-processing, and a cosine pressure A with an amplitude of 1.76 MPa is loaded within the $2\theta_0$ angle of the tire bead seat. The magnitude of the cosine pressure A remains unchanged, and the loading directions are divided into three, which are denoted as A1, A2, and A3, corresponding to orange, blue, and yellow in Fig. 19(b), respectively, and three cosine pressure simulations are loaded in the range of 36°. An inflation pressure of 0.45MPa is applied to the outer surface element between the two bead seats of the tire. Where: cosine pressure A1 faces the window, cosine pressure A2 is in the middle position, and cosine pressure A3 faces the spokes. They are respectively recorded as A1, A2, and A3 working conditions during calculation and analysis.

The radial fatigue experimental finite element model of the assembled wheel is shown in Fig 19.

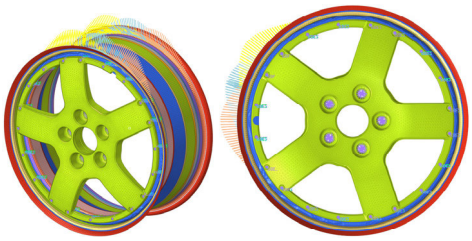

(a) Front side of the wheel (b) Reverse side of the wheel

FIGURE 19. Finite element model of radial working condition of assembled wheel.

The results of the radial fatigue analysis for the shell element model and the body element model are shown in Fig 20-23. It can be seen from the simulation calculation that when the cosine pressure is facing the middle position (A2 working condition), both the rim model of the shell element and the disc model of the body element produces the maximum stress value.The maximum stress value of the rim occurs at the bead seat cosine pressure maximum loading away from the disc side, and the maximum stress value of the disc appears at the upper middle weight reduction groove on the opposite side of the disc. The maximum stress values for both are within their respective allowable stresses, and the strength requirements of the assembled wheel are met. When the cosine pressure is directly on the spoke (case A3), the displacement offset of the rim node is the largest at the loading point away from the disc side and the maximum wheel displacement offset of the shell element and body element is 1.24mm, and 1.22mm, respectively.

The comparison results are shown in Table 4. Regarding the maximum stresses in the rim and disc, the new model and the old model not only meet the requirements, but the difference between the maximum stresses of both is less

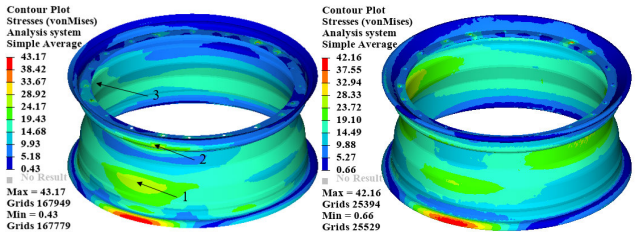

(a) Shell element model (b) Body element model

FIGURE 20. Rim stress in A_2 working condition.

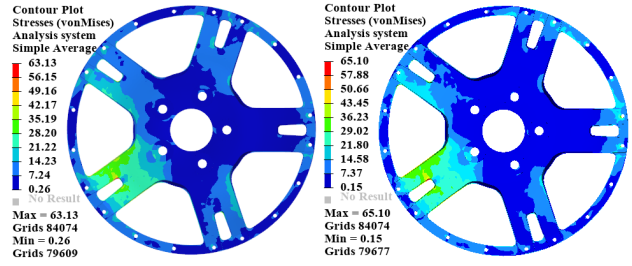

(a) Shell element model (b) Body element model

FIGURE 21. Frontal stress of wheel discs under A_2 working condition.

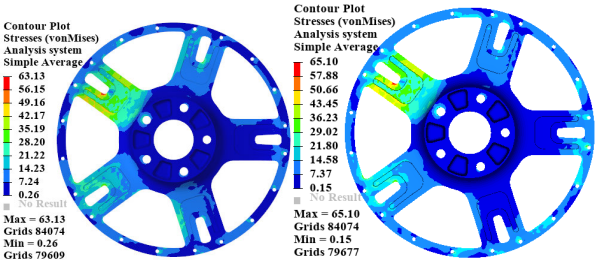

(a) Shell element model (b) Body element model

FIGURE 22. Stress on the opposite side of the discs under A_2 working condition.

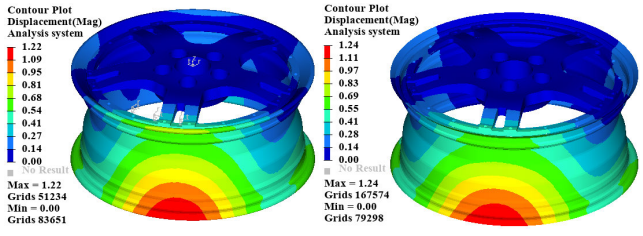

(a) Shell element model (b) Body element model

FIGURE 23. Wheel displacement under A_3 working condition.

than 5%, as well as the occurrence location, is the same, but the calculation time is reduced by 79.47%.

D. WHEEL MODAL ANALYSIS

Modal analysis is a crucial method for studying the dynamic characteristics of structures. The wheels' first-order bending and torsional modal frequencies should avoid the engine and road excitation frequencies. The free mode analysis is

TABLE 4. Comparison of radial fatigue performance of shell element models.

Performance	Shell element model	Body element model	Change rate
Maximum rim stress/MPa	43.17	42.16	2.40%
Stress at rim 1/MPa	27.77	27.76	0.04%
Stress at rim 2/MPa	25.99	25.33	2.61%
Stress at rim 3/MPa	19.20	28.82	-33.38%
Disc maximum stress/MPa	63.13	65.10	-3.03%
Maximum wheel displacement/mm	1.22	1.24	-1.61%
Calculation time/s	11.54	56.21	-79.47%

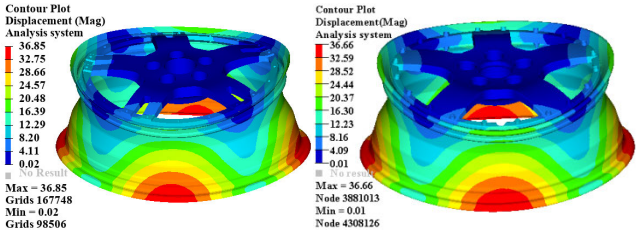

(a) Shell element model (b) Body element model

FIGURE 24. First-order bending mode.

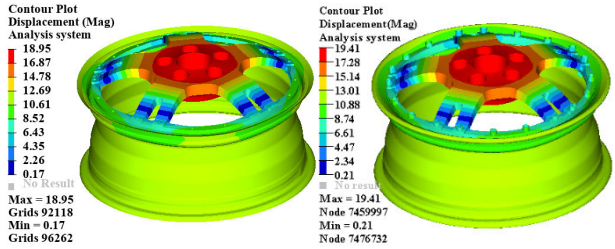

(a) Shell element model (b) Body element model

FIGURE 25. First-order torsional mode.

performed on the shell element model and the body element model respectively, and the first-order bending and first-order torsional mode vibration patterns are extracted. The results are shown in Fig 24-25, and the results of the two comparisons are shown in Table 5.

In the comparison results of Table 5, the first-order modal frequency of the shell element is lower than the first-order modal frequency of the body element, the difference is less than 5%, and the modal shapes are the same. The first-order modal frequency is much higher than the engine and road

TABLE 5. Comparison of free mode of shell element model.

Performance	Shell element model	Body element model	Change rate
First-order bending mode frequency	329.1	345.3	-4.69%
First-order torsional mode frequency	773.0	801.0	-3.50%

excitation frequency and the frequency of other car parts. This assembled wheel's low-frequency vibration characteristics meet the modal frequency requirements of automotive NVH.

V. FATIGUE LIFE ANALYSIS OF ASSEMBLED WHEELS

A. WHEEL BENDING FATIGUE LIFE ANALYSIS

Fatigue life calculations were performed using the nominal stress method, S-N curves for magnesium alloy ZK61M and aluminum alloy 6061 materials, as shown in Fig. 26.

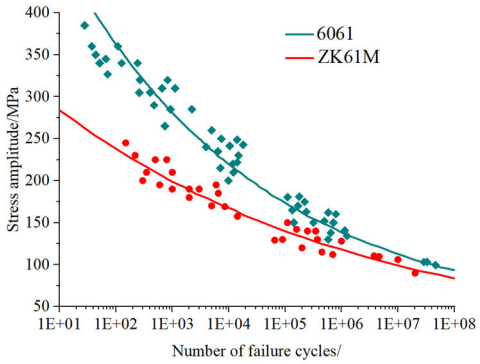

FIGURE 26. S-N curves of magnesium alloy ZK61M and aluminum alloy 6061.

The wheel rotation speed on the bending fatigue tester is 790r/min. The loading force in the bending fatigue test varies as a sinusoidal function, and the scalar is the ratio of the loading force to the maximum loading force. Then the bending fatigue test's load-time course curve is shown in Fig. 27.

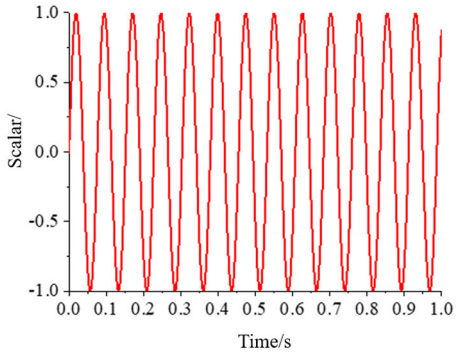

FIGURE 27. Load-time history curve of assembled wheel bending fatigue test.

Fatigue software was used to solve the bending fatigue life of the assembled wheels under F_3 conditions, and the results are shown in Fig. 28. The minimum bending fatigue life of the wheel occurs at the root weight reduction groove on the opposite side of the spokes, and the size is 230,000 times, which meets the national standard requires that the dynamic bending fatigue life of the wheel should be greater than 100,000 times. Based on the bending fatigue life results, there is still room for optimization of the assembled wheel.

B. RADIAL FATIGUE LIFE ANALYSIS OF WHEELS

The material S-N curves in section V-A. are still used for assembled wheels' radial fatigue life calculations. The wheels rotate at 50km/h on the radial fatigue tester, the wheel's rotation speed on the radial fatigue tester is 50km/h, and the radial load varies as a sinusoidal function. Then the load-time course curve of the radial fatigue test as shown in Fig 29.

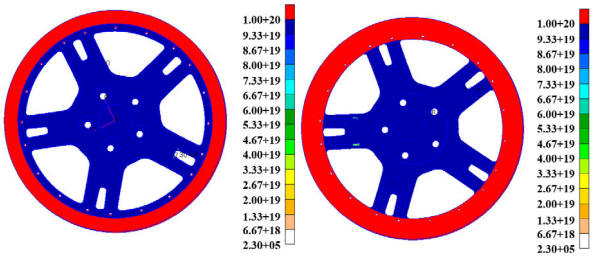

(a) Wheel front fatigue life (b) Wheel reverse fatigue life

FIGURE 28. Fatigue life cloud at maximum stress for assembled wheels.

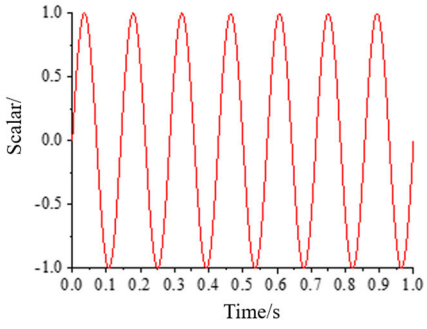

FIGURE 29. Load-time history curve of radial fatigue test of assembled wheel.

Fatigue software was used to solve the bending fatigue life of the assembled wheel under A_2 conditions with the stress combination method von Mises, and the radial fatigue life cloud of the wheel is shown in Fig. 30.

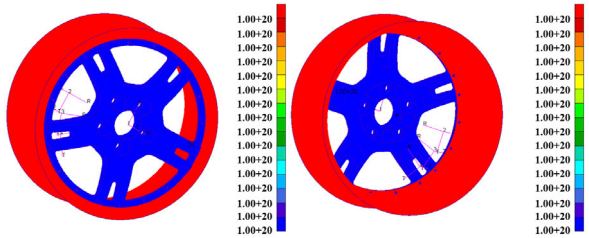

(a) Wheel front fatigue life (b) Wheel reverse fatigue life

FIGURE 30. Fatigue life cloud at maximum stress for assembled wheels.

As shown in Fig 30, the radial fatigue life of the assembled wheel is 10^{20} times, which is infinite life and meets the requirement that the test life should be greater than 500,000 times, and there is still room for further optimization of the assembled wheel.

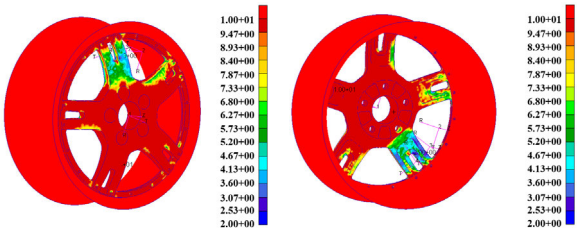

(a)Wheel front (b) The opposite side of the wheel

FIGURE 31. Cloud plot of wheel fatigue life safety factor at A_2 working condition.

A fatigue life safety factor is required to analyze the fatigue damage distribution for infinite life components. The cloud plot of fatigue life safety factor for A_2 working conditions is shown in Fig 31. As can be seen from the figure, the fatigue damage of the wheel occurs preferentially at the location where the upper part of the spokes is connected to the spoke ring, with a minimum value of 2. This meets the requirement of a safety factor greater than 1.2 in engineering, and the wheel structure can be further optimized for weight reduction.

VI. MULTI-OBJECTIVE OPTIMIZATION DESIGN OF ASSEMBLED WHEELS

A. DESIGN VARIABLE DEFINITIONS

According to the parametric model of rim and disc created in Section III, 26 design variables are defined, as shown in Fig. 32. Each design variable and the range of values are shown in Table 6.

As shown in Figure 32 and Table 6. According to the structural characteristics of the wheel, the design variables x_{17} and x_{18} are associated, and the incremental values change synchronously. The change of the design variable x_{14} changes the circumferential length of the hub weight-reducing groove. However, limited to the position of the hub bolt holes, the increment of x_{14} only changes the circumferential length of the upper part of the weight-reducing groove close to the mounting surface and the circumferential length of the lower part of the weight-reducing groove (the angle of the hub weight-reducing groove) remains unchanged.

B. CONTRIBUTION ANALYSIS

Combining the wheel bending and radial fatigue performance, 200 sample points were taken using the optimized Latin superlift method. Among them, the sampling time of the body element model is 5524.56s, and the sampling time of the shell element model is 2313.14s, which only accounts for 41.87% of the sampling time of the body element. After sampling, the contribution of each design variable to the mass was obtained by simulation, and the results are shown in Fig 33. After the results were obtained, The top 16 of contributions is taken as the design variable of multi-objective optimization.

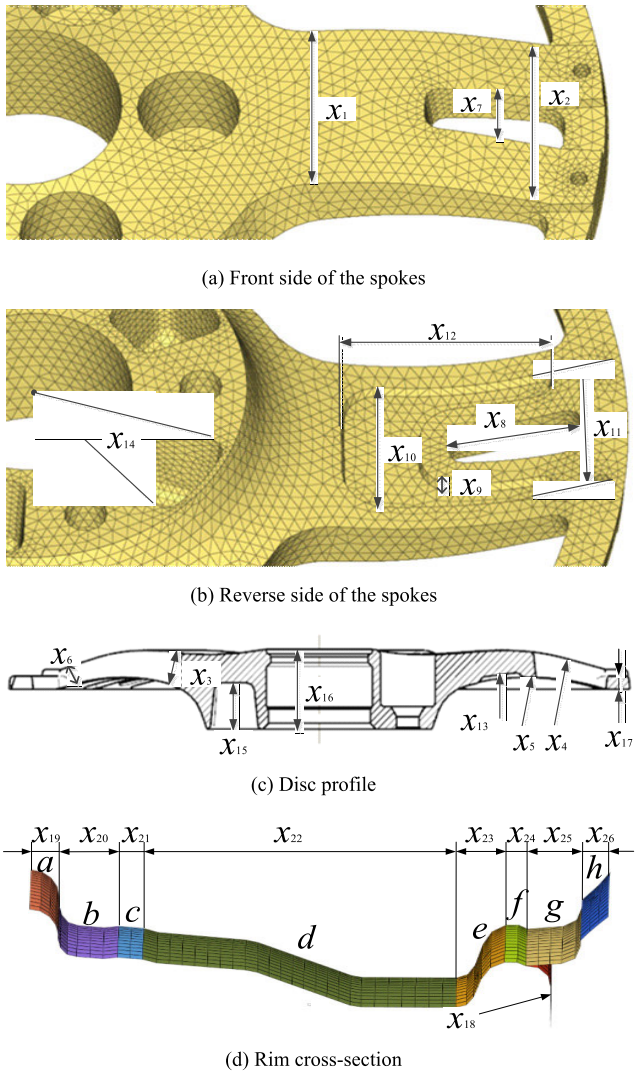

(a) Front side of the spokes

(b) Reverse side of the spokes

(c) Disc profile

(d) Rim cross-section

FIGURE 32. Schematic diagram of design variables.

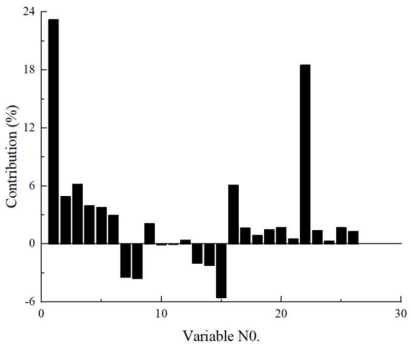

FIGURE 33. Contribution analysis of design variables.

C. APPROXIMATE MODEL BUILDING

An optimized Latin hypercube design was used to select 200 sample points, which were then used to fit Kriging and RBF approximation models. To verify the accuracy of

TABLE 6. The design variables and their value ranges.

Design Variables	Variable Description	Initial values	Lower limit	Upper limit
x_1/mm	Disc root width	68.0	61.0	75.0
x_2/mm	Disc top width	65.0	60.0	70.0
x_3/mm	Disc root thickness	18.5	13.5	23.5
x_4/mm	Radius of spokes frontal circle	150.0	135.0	165.0
x_5/mm	Spoke reverse circular diameter	156.3	140.7	171.9
x_6/mm	Disc top thickness	11.5	8.5	14.5
x_7/mm	Spoke through slot width	12.0	0.0	17.0
x_8/mm	Spoke through slot length	44.0	40.0	48.0
x_9/mm	Spoke through-slot tabs Flat Height	3.5	-3.5	3.5
x_{10}/mm	Root width of spoke weight-reducing groove	45.0	35.0	50.0
x_{11}/mm	Top width of spoke weight-reducing groove	45.0	35.0	50.0
x_{12}/mm	Length of spoke weight-reducing groove	70.0	65.0	75.0
x_{13}/mm	Spoke weight reduction groove depth	3.5	0.0	7.0
x_{14}/°	Hub weight reduction groove angle	30.0	25.0	40.0
x_{15}/mm	Hub weight reduction groove depth	29.0	23.0	35.0
x_{16}/mm	Hub thickness	48.0	36.0	52.0
x_{17}/mm	Thickness of disc ring	8.0	6.0	10.0
x_{18}/mm	Thickness of rim ring	8.0	6.0	10.0
x_{19}/mm	Thickness of rim a area	5.5	4.5	5.5
x_{20}/mm	Thickness of rim b area	5.5	4.5	5.5
x_{21}/mm	Thickness of rim c area	5.5	4.5	5.5
x_{22}/mm	Thickness of rim d area	4.5	3.5	5.5
x_{23}/mm	Thickness of rim e area	6.0	5.0	7.0
x_{24}/mm	Thickness of rim f area	6.0	5.0	7.0
x_{25}/mm	Thickness of rim g area	6.0	5.0	7.0
x_{26}/mm	Thickness of rim h area	6.0	5.0	7.0

the obtained approximation model, 20 sample points were obtained using the Hammersley experimental design and then substituted into the approximation model, and the results are shown in Fig 34

The coefficient of determination (R^2), root mean square error (RMSE), and maximum absolute relative error (MAPE) were used to assess the accuracy of the approximation model. The closer the R^2 is to 1, and the closer the RMSE and MAPE are to 0, the higher the accuracy of the proxy model is indicated. Table 6 shows the specific index values of the accuracy test results of each approximate model. As seen from Table 7, the Kriging model only has a small RMSE for the maximum stress of the discs in bending conditions, but the RMSE only represents the accuracy of the local model. In all other aspects, the accuracy of the RBF model exceeds that of the Kriging model. In summary, the RBF approximation model will be subsequently used for multi-objective optimization.

D. MULTI-OBJECTIVE OPTIMIZATION MATHEMATICAL MODEL

The multi-objective optimized design of the magnesium alloy-aluminum alloy assembled wheel is carried out by considering the performance indexes of wheel mass, strength, stiffness, modal, bending, and radial fatigue life, and the

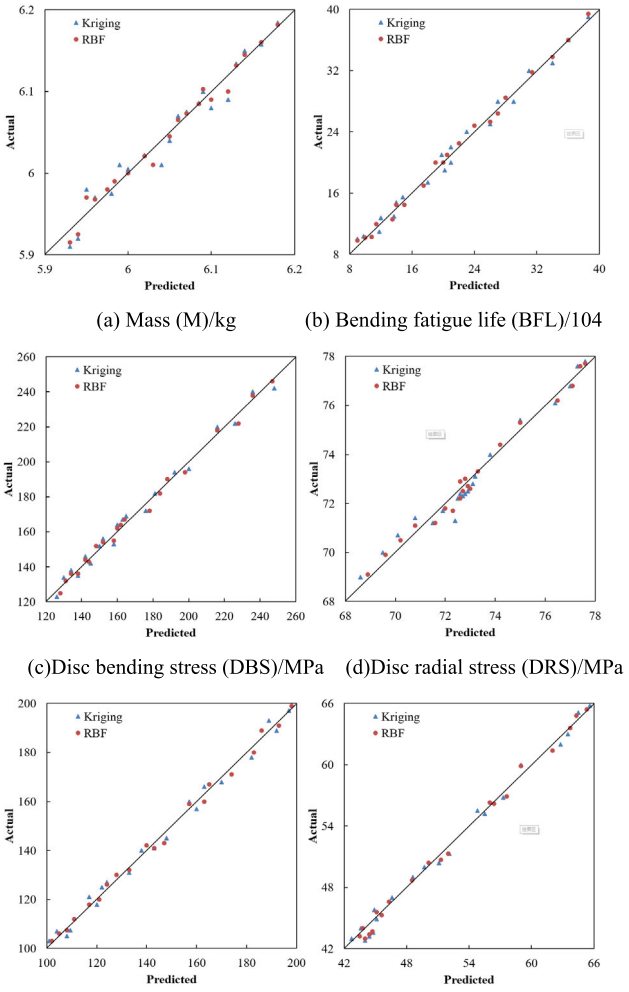

FIGURE 34. Approximate model accuracy of some performance indicators.

TABLE 7. Each design variable and its value range.

Performance	Kriging surrogate model			RBF surrogate model		
	R^2	RMSE	MAPE	R^2	RMSE	MAPE
M/Kg	0.9573	0.02606	5.017%	0.9764	0.01719	3.350%
BFL/10^4	0.9605	0.05063	10.131%	0.9786	0.03667	8.163%
DBS/MPa	0.9803	0.0227	3.268%	0.9873	0.0349	3.488%
DRS /MPa	0.9506	0.0059	1.543%	0.9806	0.0041	8.368%
RBS /MPa	0.9685	0.02304	3.306%	0.9789	0.02232	8.223%
RRS /MPa	0.9783	0.01472	2.804%	0.9823	0.01189	2.326%

optimized mathematical model is.

$$\begin{cases} \min\left(\mathrm{m}(\boldsymbol{x}), -\mathrm{N_b}(\boldsymbol{x}), \quad \sigma_{\mathrm{rr}}(\boldsymbol{x})\right) \\ \text{s.t.} \begin{cases} \sigma_{\mathrm{bd}}(\boldsymbol{x}) \le \sigma_{d0} \\ \sigma_{\mathrm{rd}}(\mathrm{x}) \le \sigma_{d0} \\ \sigma_{\mathrm{br}}(\boldsymbol{x}) \le \sigma_{r0} \\ \mathrm{s_N}(\boldsymbol{x}) \ge s_{N0} \\ \mathrm{D_b}(\boldsymbol{x}) \le D_{b0} \\ |\mathrm{C_r}(\boldsymbol{x}) - \mathrm{C}_{r0}| \le 0.1\mathrm{C}_{r0} \\ |\mathrm{f_1}(\boldsymbol{x}) - f_{10}| \le 0.15\, f_{10} \\ \mathrm{N_r}(\boldsymbol{x}) \ge N_{r0} \\ \boldsymbol{x} \in (\boldsymbol{x}_L, \boldsymbol{x}_U) \end{cases} \end{cases} \tag{15}$$

where $m(\boldsymbol{x})$ is the wheel mass, kg; $N_b(\boldsymbol{x})$ is the bending fatigue life of wheel, 10^4; $\sigma_{bd}(\boldsymbol{x})$ and $\sigma_{rd}(\boldsymbol{x})$ are disc stresses in bending and radial service, MPa; $\sigma_{br}(\boldsymbol{x})$ and $\sigma_{rr}(\boldsymbol{x})$ are the rim stresses under bending and radial conditions, MPa; σ_{d0} and σ_{r0} are the yield stresses of the discs and rims, respectively, MPa, σ_{d0}=*190MPa*, σ_{r0}=*170MPa*; $s_N(\boldsymbol{x})$ and s_{N0} are the safety factor and the permissible value of the dynamic radial fatigue life of the wheel, respectively, s_{N0}=*1.2*; $D_b(\boldsymbol{x})$ and D_{b0} are the maximum displacement and permissible displacement values of the wheel nodes under bending conditions, mm, D_{b0}=*0.8mm*; $C_r(\boldsymbol{x})$ and C_{r0} are the flexural and permissible values of the wheel in radial service, N·mm, C_{r0}=*3800N·mm*; $f_1(\boldsymbol{x})$ and f_{10} are the wheel first-order modal frequency and the initial first-order modal frequency, Hz, respectively, f_{10}=*329.1Hz*; $N_r(\boldsymbol{x})$ and N_{r0} are radial fatigue life and allowable values, 10^4, N_{r0}= 50 × 10^4 cycles; x is the design variable, x_L and is x_U the lower upper limit of the value of the design variable respectively.

VII. MULTIDISCIPLINARY AND MULTI-OBJECTIVE OPTIMIZATION

A. OPTIMIZATION PLATFORM

In the multi-objective optimization platform Isight, based on the constructed Kriging approximation model. Lightweight multi-objective optimization design of assembled wheels using modified non-dominated sorting genetic algorithm-II (MNSGA-II). The optimization platform is shown in Fig. 35.

B. OPTIMIZATION RESULTS

Combined with the RBF model, the number of MNSGA-II populations was set to 20, the number of genetic generations was 100, and the crossover probability was 0.9. After 2001 iterations of computation, the Pareto frontier consisting of 300 non-dominated optimal solutions is obtained, as shown in Fig 36.

From the Pareto frontier, it is clear that the performance of wheel mass, bending fatigue life, and radial stress on the rim are challenging to optimize at the same time, so different compromises need to be selected for different optimization

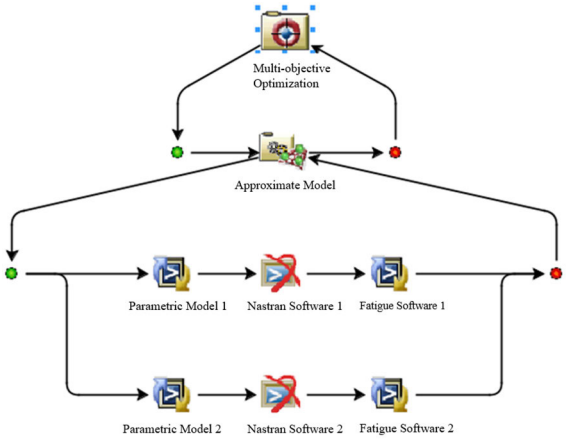

FIGURE 35. Wheel multi-objective optimization design platform.

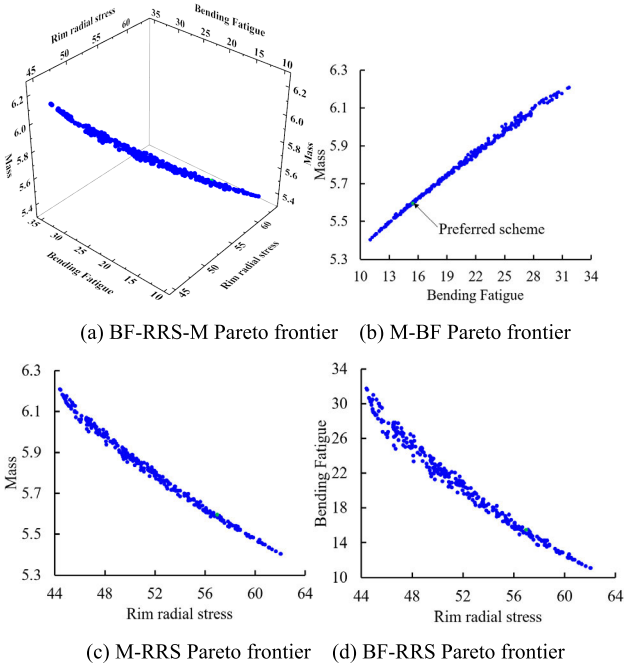

FIGURE 36. Pareto frontier after optimization design.

needs. According to the entropy weight grey relation analysis method in section II-A, the weights of the three under the entropy weight method are 0.244,0.297, and 0.459 by using the formula (9). The grey relation degree of each scheme is obtained according to equation (5), and the results are shown in Fig 37. Among them, the grey relation degree of the 149th non-dominated scheme is 0.8881, the largest among all schemes.

The lightweight multi-objective optimized design solution was determined based on the preferred compromise solution. The optimization results of each design variable were compared with the initial values, as shown in Table 8. The design variable x_7 becomes 0, indicating the disappearance of the wheel disc through-slots after optimization, which will

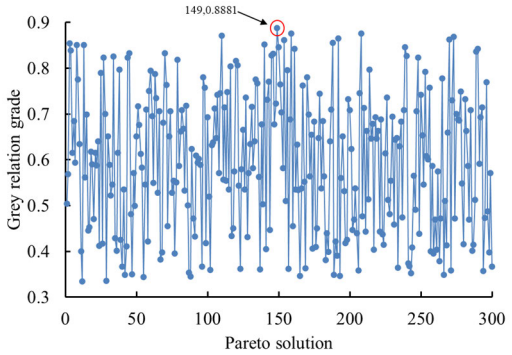

FIGURE 37. Grey relational degree of Pareto frontier.

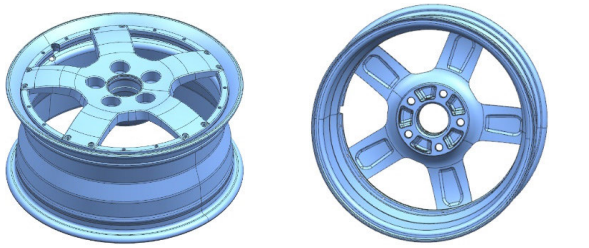

FIGURE 38. 3D model of assembled wheel after multi-objective optimization design.

TABLE 8. Optimization results of design variables.

Design Variables	Variable Descriptions	Initial Values	Preferred values
x_1/mm	Disc root width	68.0	61.0
x_2/mm	Disc top width	65.0	60.0
x_3/mm	Disc root thickness	18.5	13.5
x_4/mm	Radius of spokes frontal circle	150.0	152.12
x_5/mm	Spoke reverse arc diameter	156.3	153.69
x_6/mm	Disc top thickness	11.5	8.5
x_7/mm	Spoke through slot width	12.0	0.0
x_8/mm	Length of spokes through groove	44.0	40.0
x_9/mm	Spoke through-slot tabs Flat Height	3.5	-2.5
x_{10}/mm	Root width of spoke weight-reducing groove	45.0	36.82
x_{11}/mm	Top width of spoke weight-reducing groove	45.0	43.12
x_{12}/mm	Length of spoke weight-reducing groove	70.0	73.10
x_{13}/mm	Spoke weight reduction groove depth	3.5	6.0
x_{14}/°	Hub weight reduction groove angle	30.0	25.0
x_{15}/mm	Hub weight reduction groove depth	29.0	23.0
x_{16}/mm	Hub thickness	48.0	36.0
x_{17}/mm	Thickness of disc ring	8.0	6.0
x_{18}/mm	Thickness of rim ring	8.0	6.0
x_{19}/mm	Thickness of rim a area	5.5	4.82
x_{20}/mm	Thickness of rim b area	5.5	4.82
x_{21}/mm	Thickness of rim c area	5.5	4.82
x_{22}/mm	Thickness of rim d area	4.5	4.14
x_{23}/mm	Thickness of rim e area	6.0	6.13
x_{24}/mm	Thickness of rim f area	6.0	5.21
x_{25}/mm	Thickness of rim g area	6.0	5.03
x_{26}/mm	Thickness of rim h area	6.0	5.50

enhance the wheel's strength at the disc-rim joint, significantly improving the radial fatigue performance of the wheel.

As shown in Table 8, the design variable x7 becomes 0. It shows that the spoke groove disappears after optimization, which will enhance the strength of the connection between the disc and the rim of the wheel, significantly improving the radial fatigue performance. According to the values of the design variables in Table 8, the 3D modeling of the assembled wheel is re-established. The 3D model of the assembled wheel after lightweight multi-disciplinary and multi-objective optimization design is shown in Figure 38.

According to the optimization results of each performance index of the compromise solution, as shown in Table 8. The finite element model of the optimized assembled wheel is analyzed and calculated respectively, and the simulation values of each performance index are obtained. The preferred values are compared with the simulation values, as shown in Table 9.

As shown in Table 9, the preferred values are very close to the simulated values, with a maximum error of 5.1%. The optimization accuracy meets the requirements, which verifies the accuracy of the approximation model and the compromise solution obtained by the MNSGA-II genetic algorithm. The mass of the optimized 3D model of the assembled wheel becomes 5.635 kg. The multi-objective optimization resulted in a 10.17% reduction in wheel mass and 0.638kg weight reduction compared to the joint topology optimization.

TABLE 9. Comparison of pareto front solution and optimized simulation values.

Contrast items	Preferred values	Simulation values	Error values
m (x) /kg	5.593	5.635	-0.7%
N_b (x) /10^4	15.5	15.2	1.9%
σ_{bd}/MPa	142.31	148.13	-3.9%
σ_{rd}/MPa	55.74	53.01	5.1%
σ_{br}/MPa	128.49	135.14	-4.9%
σ_{rr}/MPa	46.71	45.89	1.8%
D_b (x) /mm	0.81	0.79	2.5%
C_r (x) /N·mm	4121	3936	4.7%
$f_{1(x)}$	277.4	283.2	-2.0%
S_N (x)	1.63	1.67	-2.4%
Nr (x) /10^4	10^{16}	10^{16}	

VIII. COMPARATIVE ANALYSIS OF PERFORMANCE OF ASSEMBLED WHEEL BEFORE AND AFTER OPTIMIZATION

A. COMPARISON OF BENDING FATIGUE PERFORMANCE CLOUD IMAGES

The bending fatigue performance of the assembled wheel before and after optimization was compared and analyzed. The stress and nodal displacement cloud diagram of the optimized wheel is shown in Figure 39. The cloud diagram of bending fatigue life is shown in Figure 40.

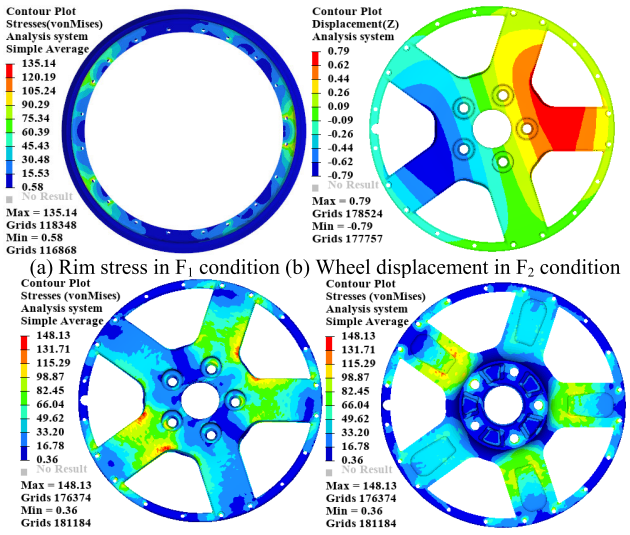

(a) Rim stress in F_1 condition (b) Wheel displacement in F_2 condition

(c) Front disc stress in F_3 condition (d) Back disc stress in F_3 condition

FIGURE 39. Stress and nodal displacement clouds of the optimized wheel.

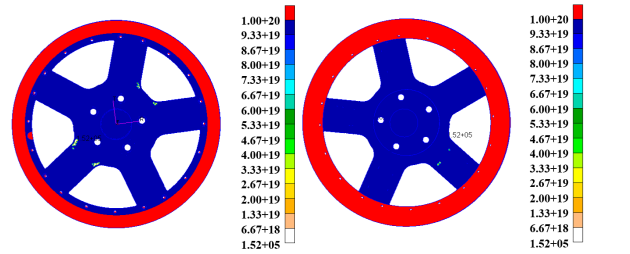

(a) Fatigue life of wheel front (b) Fatigue life of wheel reverse side

FIGURE 40. Fatigue life of wheel at F3 operating condition after optimization.

TABLE 10. Comparison results of bending fatigue performance index before and after optimization.

Performance Index	Symbols/ Elements	Before Optimization	After Optimization	Change Rate/%
Disc Stress	σ_{bd}/MPa	133.57	148.13	10.90
Rim Stress	σ_{br}/MPa	126.38	135.14	6.93
Nodal Displacement	$D_b(x)/mm$	0.70	0.79	12.86
Fatigue Life	$N_b(x)/10^4$	23.0	15.20	-51.32

Table 10 compares bending fatigue performance before and after optimization, combined with Figures 39-40. After optimization, the wheel stress and nodal displacement both increase, reducing the wheel's bending fatigue life. However, the optimization of the size of the spoke weight-reducing groove improves the stress on the weight-reducing groove at the root of the back of the spoke so that the minimum bending fatigue life of the wheel changes from the back of the spoke root to the front, and the minimum fatigue life is 152,000 times. After optimization, all the bending fatigue performance indexes of the assembled wheel meet the design requirements.

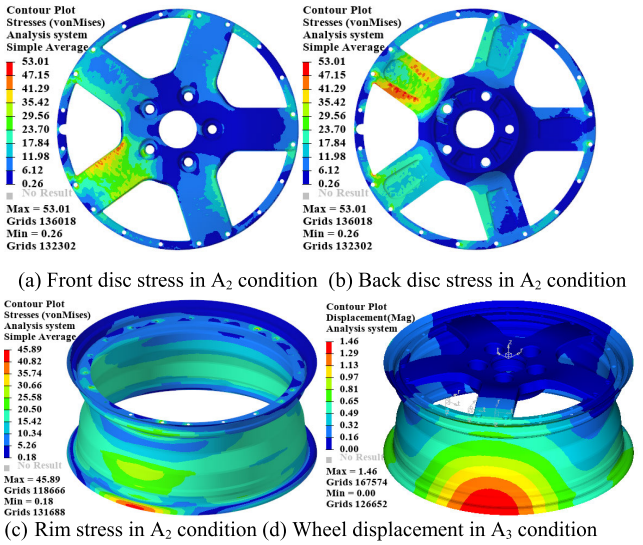

(a) Front disc stress in A_2 condition (b) Back disc stress in A_2 condition

(c) Rim stress in A_2 condition (d) Wheel displacement in A_3 condition

FIGURE 41. Stress and nodal displacement nephogram of optimized wheel.

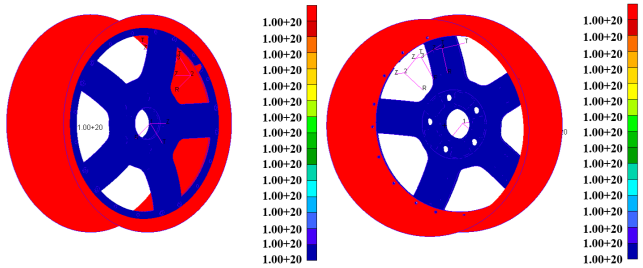

(e) Wheel front fatigue life (f) Wheel reverse fatigue life

FIGURE 42. Fatigue life of optimized rear wheel under A2 condition.

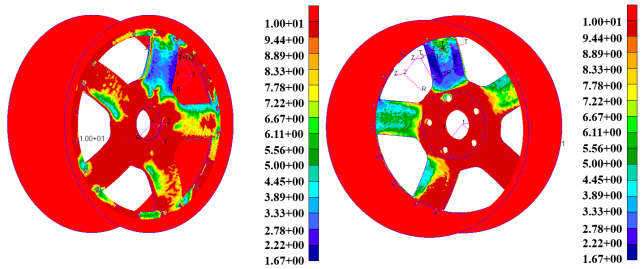

(a) Front of wheel model (b) Back of wheel model

FIGURE 43. Safety factor of wheel fatigue life under optimized A2 condition.

B. COMPARISON OF RADIAL FATIGUE PERFORMANCE CLOUDS

The radial fatigue performance of assembled wheels before and after optimization is compared and analyzed. The optimized assembly wheel stress and nodal displacement cloud diagram are shown in Fig. 41. The cloud charts of radial fatigue life and safety factor of radial fatigue life are shown in Fig. 42-43, respectively.

TABLE 11. Comparison results of radial fatigue performance indexes before and after optimization.

Performance Index	Symbol / Element	Before Optimization	After Optimization	Change Rate / %
Disc Stress	σ_{rd}/MPa	63.13	53.01	-16.03
Rim Stress	σ_{rr}/MPa	43.17	45.89	6.30
Nodal Displacement	$D_r(x)/mm$	1.24	1.46	17.74
Fatigue Life	$N_r(x)/10^4$	10^{16}	10^{16}	
Safety Factor	$S_N(x)$	2.0	1.67	-16.50

Table 11 gives the comparison results of radial fatigue performance indexes before and after optimization. Combined with Fig 41-43, the change in the parameters of the disc through slot and the spoke weight reduction slot results in a reduction in the stress on the spokes. The reduction of rim thickness makes the nodal displacement and the rim stress larger. The minimum fatigue life safety factor occurs at the disc ring to wheel bar connection with a minimum value of 1.67. After optimization, all the radial fatigue performance indexes of the assembled wheel meet the standard requirements.

C. MODAL PERFORMANCE COMPARISON

The first-order bending and torsional modes of the assembled wheel after optimization are shown in Fig. 44, and a comparative analysis of the assembled wheel modes before and after optimization is performed. The modal frequencies are compared in Table 12, where the wheel's rim and the spoke root size reduction have a more significant effect on the modal frequencies. The optimized first-order modal frequencies are reduced, but they all satisfy the constraint requirements of low-frequency intrinsic vibration patterns and automotive NVH (Noise, Vibration, harshness) modal frequency requirements.

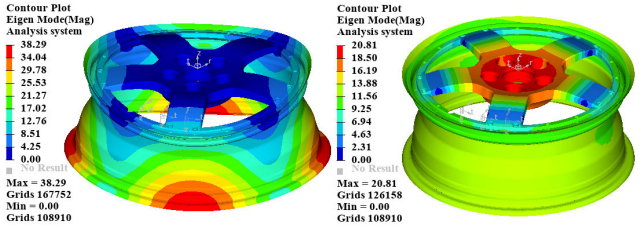

(a) First-order bending mode (b) First-order torsional mode

FIGURE 44. Optimized first-order bending and torsion modes of wheels.

IX. DYNAMIC FATIGUE TEST PERFORMANCE ANALYSIS AND FINITE ELEMENT VERIFICATION

A. DYNAMIC BENDING FATIGUE TEST

Based on the finite element results of the dynamic bending fatigue test of the wheel, the strain test points were selected on the wheel, and the wheel was mounted on the bending fatigue tester, and the test equipment was connected to the instrument, as shown in Fig 45.

TABLE 12. Comparison results of modal frequencies before and after optimization.

performance index	Before optimization	After optimization	Change rate / %
First-order bending modal frequency	329.1	283.2	-13.95
First-order torsional modal frequency	773.0	742.5	-3.95

FIGURE 45. Test equipment and instrument connection.

Each cycle a certain number of times to take off the wheel for color penetration method for flaw detection. Bending fatigue damage occurred in the wheel after 160,000 cycles, and the test results met the requirements, and the damage site and cracks are shown in Fig 46.

(a) Global graph (b) Detail image

FIGURE 46. Wheel bending fatigue damage location and crack.

The crack of the wheel after the test occurred at the location of the root of the front side of the spokes, which is consistent with the location of the fatigue damage analyzed by the finite element simulation. The simulation value of wheel bending fatigue life is 152,000 cycles, and the error is -5% compared with the test result, which proves the accuracy of the finite element analysis results.

B. DYNAMIC RADIAL FATIGUE TEST

Based on the finite element results of the dynamic radial fatigue test of the wheel, strain test points were selected on the wheel, the wheel was mounted on the radial fatigue tester, and the test equipment was connected to the instrument, as shown in Fig. 47.

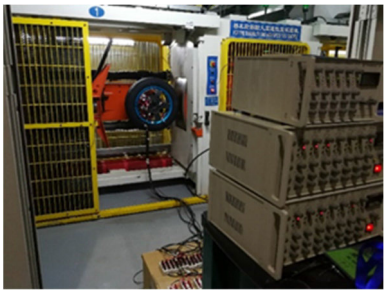

FIGURE 47. Test equipment and instrument connection.

Each cycle a certain number of times to take off the wheel for color penetration method for flaw detection. Wheel bending fatigue damage occurred after 500,000 cycles. The test results meet the requirements of national standards, and the damage site and cracks are shown in Fig. 48.

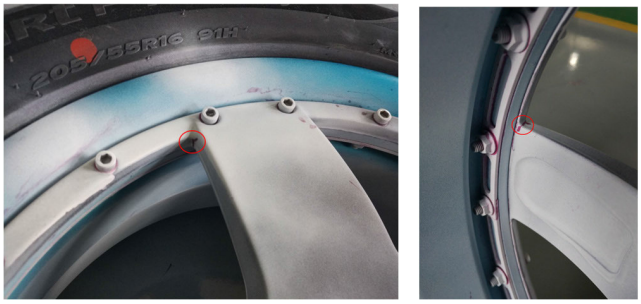

(a) Front view (b) Side view

FIGURE 48. Radial fatigue damage parts and cracks of wheels.

The crack occurred at the joint between the disc ring and the wheel bar, and the location of the test crack was consistent with the simulation results, further illustrating the accuracy of the FEA (Finite Element Analysis) results.

X. CONCLUSION

This paper constructs a finite element analysis model of the wheel with the combination of shell-body element. We propose an assembled wheel design method with a magnesium alloy rim-aluminum alloy disc structure. Proposed a hybrid method of entropy-weighted grey relation analysis (EGRA) combined with modified non-dominated sorting genetic algorithm-II (MNSGA-II), multi-objective optimization of assembled wheels combined with approximate model approach and ranking and filtering of optimized solution sets, and finally, experimental validation was performed. This paper combines the optimization methods in the wheel's conceptual and detailed design phases. We propose a combination of multi-operational joint topology optimization and multi-objective optimization of the assembled wheel. It realizes the advantageous combination of different design stages, parts, and optimization design methods. We provide a way and technical basis for multi-objective optimization and design of wheel lightweight.

1) A conceptual design model of the wheel was developed with the 16 × 6$^1/_2$J type wheel as the research object. The topology optimization models of the wheel under bending and radial fatigue test conditions were established, respectively, and the joint topology optimization method of the wheel disc based on the two conditions was proposed to obtain the disc topology with optimal overall performance.
2) Based on the topology of wheel discs and rim design criteria, combined with the implicit parameterization technology, SFE-Concept software is used to establish the implicit parameterization model of the rim. An assembled wheel consisting of a magnesium alloy rim and an aluminum alloy spoke connected by bolts was designed. The performance parameters such as stress, displacement, life and life safety factor of assembled wheels under bending and radial fatigue conditions, and modal frequency are analyzed to study the influence of wheel structure parameters on each performance index.
3) Parametric models for fatigue analysis of assembled wheels were created using DEP-MeshWorks and SFE-Concept software, Design of experiment (DOE) sampling was performed, and 21 design variables were screened in combination with the contribution analysis method. A hybrid method of entropy-weighted grey relation analysis (EGRA) combined with a modified non-dominated sorting genetic algorithm-II (MNSGA-II) is proposed to obtain the Pareto frontier solution set by combining an approximate model approach for multi-objective optimization of assembled wheels. The EGRA method ranks the Pareto solution set and filters out the optimal compromise solution.
4) The performance indicators of the assembled wheels before and after optimization were compared by simulation analysis, and experimental verification was carried out. The results show that all the indicators of fatigue performance of the assembled wheel have been reasonably modified, and the weight reduction of the wheel is 10.17%, which is a significant effect of lightweight. The hybrid method proposed in this paper with entropy-weighted grey relation analysis (EGRA) combined with modified non-dominated sorting genetic algorithm-II (MNSGA-II) can sufficiently synthesize the performance indexes of the wheel. Under guaranteed computational accuracy, the combined wheel shell-body element model proposed in this paper saves at least 46.44% of the computational time compared with the body element model.

REFERENCES

[1] H. T. Zhang, "Lightweight and performance of anti-collision strength of automobiles based on carbon fiber composites," *Korean J. Mater. Res.*, vol. 29, no. 9, pp. 525–531, Sep. 2019, doi: 10.3740/MRSK.2019.29.9.525.

[2] Z. Ding, H. Fang, B. Liu, Z. Yao, and J. Liu, "Research on the optimal scheme of 3E game for lightweight body-in-white under environmental protection policy," *Adv. Mech. Eng.*, vol. 13, no. 8, Aug. 2021, Art. no. 168781402110378, doi: 10.1177/16878140211037822.

[3] A. Hirano, "Study on wheel stiffness considering balance between driving stability and weight," *SAE Int. J. Commercial Vehicles*, vol. 8, no. 1, pp. 205–212, Apr. 2015, doi: 10.4271/2015-01-1755.

[4] W. Song, J. L. Woods, R. T. Davis, J. K. Offutt, E. P. Bellis, E. S. Handler, C. K. Sullivan, and T. W. Stone, "Failure analysis and simulation evaluation of an Al 6061 alloy wheel hub," *J. Failure Anal. Prevention*, vol. 15, no. 4, pp. 521–533, Jun. 2015, doi: 10.1007/s11668-015-9969-9.

[5] Y. Q. Wang, X. H. Liu, J. S. Chen, Y. F. Han, H. R. Meng, and N. Xiao, "Lightweight design and multi-objective optimization of steel assembled wheel," *J. Harbin Inst. Technol.*, vol. 52, no. 7, pp. 170–178, Jul. 2020, doi: 10.11918/201909211.

[6] X. Jiang, H. Liu, R. Lyu, Y. Fukushima, N. Kawada, Z. Zhang, and D. Ju, "Optimization of magnesium alloy wheel dynamic impact performance," *Adv. Mater. Sci. Eng.*, vol. 2019, pp. 1–12, Sep. 2019, doi: 10.1155/2019/2632031.

[7] W. Xu and D. Wang, "Fatigue/impact analysis and structure–connection–performance integration multi-objective optimization of a bolted carbon fiber reinforced polymer/aluminum assembled wheel," *Composites B, Eng.*, vol. 243, Aug. 2022, Art. no. 110103, doi: 10.1016/j.compositesb.2022.110103.

[8] Z. Guiju and X. Caiyuan, "Study on lightweight design of aluminium alloy wheels," *Austral. J. Mech. Eng.*, vol. 16, no. sup1, pp. 30–36, Jan. 2019, doi: 10.1080/1448837X.2018.1545469.

[9] S. Czypionka and F. Kienhöfer, "Weight reduction of a carbon fibre composite wheel," *Sci. Eng. Compos. Mater.*, vol. 26, no. 1, pp. 338–346, Aug. 2019, doi: 10.1515/secm-2019-0018.

[10] Z. M. Wang and J. Cheng, "Research and implementation of mesh model deformation simulation technology," in *Proc. 5th Annu. Int. Conf. Inf. Syst. Artif. Intell.*, vol. 1575, 2020, Art. no. 012045, doi: 10.1088/1742-6596/1575/1/012045.

[11] H. Fang, C. Y. Gong, C. H. Yu, C. W. Min, X. Zhang, J. Liu, and L. Q. Xiao, "Efficient mesh deformation based on Cartesian background mesh," *Comput. Math. Appl.*, vol. 73, no. 1, pp. 71–86, Jan. 2017, doi: 10.1016/j.camwa.2016.10.023.

[12] L. Xie, Z. Kang, H. Hong, Z. Qiu, and B. Jiang, "Local mesh deformation using a dual-restricted radial basis functions method," *Aerosp. Sci. Technol.*, vol. 130, Nov. 2022, Art. no. 107940, doi: 10.1016/j.ast.2022.107940.

[13] D. Wang, S. Zhang, and W. Xu, "Multi-objective optimization design of wheel based on the performance of 13° and 90° impact tests," *Int. J. Crashworthiness*, vol. 24, no. 3, pp. 336–361, May 2019, doi: 10.1080/13588265.2018.1451229.

[14] L. Duan, N.-C. Xiao, Z. Hu, G. Li, and A. Cheng, "An efficient lightweight design strategy for body-in-white based on implicit parameterization technique," *Structural Multidisciplinary Optim.*, vol. 55, no. 5, pp. 1927–1943, May 2017, doi: 10.1007/s00158-016-1621-0.

[15] D. F. Wang, F. Ji, S. M. Chen, Y. S. Li, H. B. Chen, and X. M. Zhao, "Implicit parameterization modeling and validation for body-in-white of a car," *Appl. Mech. Mater.*, vols. 365–366, pp. 429–434, Aug. 2013, doi: 10.4028/www.scientific.net/AMM.365-366.429.

[16] X. Chen, F. Ma, D. Wang, and C. Xie, "Carbody structural lightweighting based on implicit parameterized model," *Chin. J. Mech. Eng.*, vol. 27, no. 3, pp. 483–487, May 2014, doi: 10.3901/CJME.2014.03.483.

[17] W. M. Yao, K. F. Cai, and Y. W. Xu, "Optimizing the beam-like structure of a vehicle body using the grey–fuzzy–Taguchi method," *Eng. Optim.*, vol. 53, no. 1, pp. 49–70, Jan. 2021, doi: 10.1080/0305215X.2019.1698033.

[18] J. Liu, S. Wang, and G. Wang, "Mathematical modeling and multivariable optimization design of SUV chassis structure based on SFE CONCEPT," *Secur. Commun. Netw.*, vol. 2022, pp. 1–14, Apr. 2022, doi: 10.1155/2022/3699708.

[19] T. C. Bora, V. C. Mariani, and L. D. S. Coelho, "Multi-objective optimization of the environmental-economic dispatch with reinforcement learning based on non-dominated sorting genetic algorithm," *Appl. Thermal Eng.*, vol. 146, pp. 688–700, Jan. 2019, doi: 10.1016/j.applthermaleng.2018.10.020.

[20] M. Akbari, M. H. Shojaeefard, P. Asadi, and A. Khalkhali, "Hybrid multi-objective optimization of microstructural and mechanical properties of B4C/A356 composites fabricated by FSP using TOPSIS and modified NSGA-II," *Trans. Nonferrous Met. Soc. China.*, vol. 27, no. 11, pp. 2317–2333, Nov. 2017, doi: 10.1016/S1003-6326(17)60258-9.

[21] X. Xu, J. Chen, Z. Lin, Y. Qiao, X. Chen, Y. Zhang, Y. Xu, and Y. Li, "Optimization design for the planetary gear train of an electric vehicle under uncertainties," *Actuators*, vol. 11, no. 2, p. 49, Feb. 2022, doi: 10.3390/act11020049.

[22] F. Xiong, D. Wang, S. Chen, Q. Gao, and S. Tian, "Multi-objective lightweight and crashworthiness optimization for the side structure of an automobile body," *Structural Multidisciplinary Optim.*, vol. 58, no. 4, pp. 1823–1843, Oct. 2018, doi: 10.1007/s00158-018-1986-3.

[23] D. Wang, R. Jiang, and Y. Wu, "A hybrid method of modified NSGA-II and TOPSIS for lightweight design of parameterized passenger car subframe," *J. Mech. Sci. Technol.*, vol. 30, no. 11, pp. 4909–4917, Nov. 2016, doi: 10.1007/s12206-016-1010-z.

[24] F. Xiong, D. Wang, Z. Ma, T. Lv, and L. Ji, "Lightweight optimization of the front end structure of an automobile body using entropy-based grey relational analysis," *Proc. Inst. Mech. Eng., D, J. Automobile Eng.*, vol. 233, no. 4, pp. 917–934, Mar. 2019, doi: 10.1177/0954407018755844.

[25] S. Zhang, K. Liu, S. Zhang, and L. Xu, "Study on aerodynamic performance and lightweight multiobjective optimization design of wheel with entropy weighted grey relational analysis methods," *IEEE Access*, vol. 10, pp. 93421–93438, 2022, doi: 10.1109/ACCESS.2022.3203177.

[26] X. Zhao, P. Gao, Z. Zhang, Q. Wang, and F. Yan, "Fatigue characteristics of the extruded AZ80 automotive wheel," *Int. J. Fatigue*, vol. 132, Mar. 2020, Art. no. 105393, doi: 10.1016/j.ijfatigue.2019.105393.

[27] D. Shang, X. Liu, Y. Shan, and E. Jiang, "Research on the stamping residual stress of steel wheel disc and its effect on the fatigue life of wheel," *Int. J. Fatigue*, vol. 93, pp. 173–183, Dec. 2016, doi: 10.1016/j.ijfatigue.2016.08.020.

[28] Q. Jiang, Z. Zhao, Z. Xu, J. Sun, X. Chen, B. Su, Z. Zhao, and W. Jiang, "Effect of residual stresses on wheel fatigue life and experimental validation," *Machines*, vol. 10, no. 10, p. 924, Oct. 2022, doi: 10.3390/machines10100924.

[29] X. Wan, Y. Shan, X. Liu, H. Wang, and J. Wang, "Simulation of biaxial wheel test and fatigue life estimation considering the influence of tire and wheel camber," *Adv. Eng. Softw.*, vol. 92, pp. 57–64, Feb. 2016, doi: 10.1016/j.advengsoft.2015.11.005.

[30] Y.-C. Duan, F.-F. Zhang, D. Yao, J.-H. Hu, R. Dong, X. Zhao, and Y.-P. Guan, "Multiscale fatigue-prediction method to assess life of A356-T6 alloy wheel under biaxial loads," *Eng. Failure Anal.*, vol. 130, Dec. 2021, Art. no. 105752, doi: 10.1016/j.engfailanal.2021.105752.

[31] L. Chen, S. Li, H. Chen, D. M. Saylor, and S. Tong, "Study on the design method of equal strength rim based on stress and fatigue analysis using finite element method," *Adv. Mech. Eng.*, vol. 9, no. 3, Mar. 2017, Art. no. 168781401769269, doi: 10.1177/1687814017692698.

[32] D. Wang and W. Xu, "Fatigue failure analysis and multi-objective optimisation for the hybrid (bolted/bonded) connection of magnesium–aluminium alloy assembled wheel," *Eng. Failure Anal.*, vol. 112, May 2020, Art. no. 104530, doi: 10.1016/j.engfailanal.2020.104530.

[33] R. L. Hardy, "Multiquadric equations of topography and other irregular surfaces," *J. Geophys. Res.*, vol. 76, no. 8, pp. 1905–1915, Mar. 1971, doi: 10.1029/JB076i008p01905.

[34] T. W. Simpson, T. M. Mauery, J. J. Korte, and F. Mistree, "Kriging models for global approximation in simulation-based multidisciplinary design optimization," *AIAA J.*, vol. 39, no. 12, pp. 2233–2241, Dec. 2001, doi: 10.2514/2.1234.

SHUAI ZHANG received the B.S. and M.S. degrees in automotive engineering from the Henan University of Science and Technology, Luoyang, China, in 2011 and 2014, respectively, and the Ph.D. degree in automotive engineering from Jilin University, Jilin, China, in 2018. Since 2018, he has been a Lecturer with the College of Vehicle and Traffic Engineering, Henan University of Science and Technology. His research interests include research and innovation of automobile structure design theory and key technology.

RUIXU LI received the bachelor's degree in vehicle engineering from the Henan University of Science and Technology, Luoyang, China, where he is currently pursuing the master's degree in vehicle engineering. His research interest includes lightweight technology of automobile structure.

DONGZHEN LU received the B.S. degree in automotive engineering from Xinxiang University, Xinxiang, China, in 2021. He is currently pursuing the M.S. degree with the Henan University of Science and Technology, Luoyang, China. His research interest includes lightweight technology of automobile structure.

LIYOU XU received the B.S. degree in mechanical manufacturing technology and equipment from the Jiaozuo Institute of Technology, Jiaozuo, China, in 1998, the Ph.D. degree in vehicle engineering from the Xi'an University of Technology, Xi'an, in 2007, and the M.S. degree in vehicle engineering from the Luoyang Institute of Technology, Luoyang, China, in 2018. Since 2013, he has been a Professor with the College of Vehicle and Traffic Engineering, Henan University of Science and Technology, Luoyang. His research interests include new transmission theory and control technology, vehicle performance analysis method and simulation technology, and low-speed electric vehicle transmission technology.

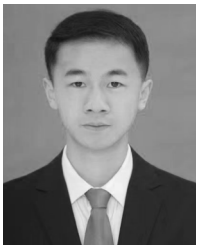

WENCHAO XU received the B.S. and M.S. degrees in vehicle engineering from the Anhui University of Technology, Huainan, in 2014 and 2017, respectively, and the Ph.D. degree in vehicle engineering from Jilin University, Jilin, China, in 2021. His research interests include research and innovation of automobile structure design theory and key technology.